

Article

High Hardness Nanocrystalline Invar Alloys Prepared from Fe-Ni Nanoparticles

Ping-Zhan Si^{1,2,*} and Chul-Jin Choi^{1,*}

¹ Powder & Ceramic Division, Korea Institute of Materials Science, Changwon, Gyeongnam 51508, Korea

² College of Materials Science and Engineering, China Jiliang University, Hangzhou 310018, China

* Correspondence: pzzi@cjl.u.edu.cn (P.-Z.S.); cjchoi@kims.re.kr (C.-J.C.);
Tel.: +82-55-280-3597 (P.-Z.S.); +82-55-280-3532 (C.-J.C.)

Received: 24 November 2017; Accepted: 25 December 2017; Published: 2 January 2018

Abstract: High-density (>98% of full density) nanocrystalline invar alloys with significantly enhanced hardness (>240 in Vicker's hardness) were prepared by sintering compacted Fe-Ni nanoparticles in hydrogen. The precursor Fe-Ni nanoparticles were synthesized by hydrogen plasma evaporation of bulk Fe₆₁Ni₃₉ alloys. The size and the productivity of the Fe-Ni nanoparticles increased with increasing hydrogen pressure. The presence of surface oxidation of the Fe-Ni nanoparticles when exposed to air was proved by the X-ray photoelectron spectra measurements. The compacted Fe-Ni nanoparticles grew rapidly at 956 °C, while the oxide impurities were removed completely by following hydrogen at 735 °C, which was found to be optimum for the synthesis of oxide-free nanocrystalline metals with fine grain size. The typical hardness of an invar alloy prepared by melting method was around 140 HV. The significantly enhanced hardness of our nanocrystalline invar alloys was potentially important in strengthening the durability of its components in instruments and in improving its machinability when machining for a component.

Keywords: nanostructured materials; invar alloy; nanocrystalline; hardness

1. Introduction

Iron-nickel invar alloys, first discovered by Guillaume in 1897 [1], have the lowest thermal expansion among all metals and alloys over a wide temperature range. The anomalously low coefficients of thermal expansion make invar alloys widely used where high dimensional stability with variation in temperature is required, such as precision instruments, hairsprings in watches, seismic creep gauges, television shadow-mask frames, valves in engines, pistons in cylinders, optical and laser measuring systems, bimetallic strips, composite manufacturing, cryogenic engineering, aeronautical and aerospace engineering, and so on [2,3]. The hardness of the invar alloy is important for the durability of the components in instruments. The typical hardness of an invar alloy, usually prepared by melting method, is around 140 HV [4]. The invar components are conventionally manufactured by machining which is expensive and difficult because the invar materials are soft and gummy. Machining bulk invar materials into complex shapes is thus particularly challenging. Additive manufacturing is an alternative method for making components with complex shapes and the typical hardness of the products make almost no change [2,4]. In this work, nanocrystalline invar alloys with significantly enhanced hardness up to 242 HV have been made. The high hardness of invar alloy is potentially important not only in strengthening the durability of its components in instruments, but also in improving its machinability when machining for a component.

It is known that the nanocrystalline materials usually exhibit improved mechanical properties such as high strength and hardness [5]. Grain refinement can be achieved by severe plastic deformation of bulk alloy or physical deposition process [6]. Electrodeposition method is also effective in preparation of nanocrystalline invar alloys [7,8]. One of the most common ways for production of nanocrystalline

metals is high-pressure compaction of nanometer-sized clusters [9,10]. Consolidation of nanocrystalline powders into fully dense materials must not alter the nanostructure in order to retain the unique properties of fine particles. However, recrystallization and grain-growth occur readily during high temperature annealing process. Nanocrystalline powders can also be produced using other methods like mechanical alloying [11,12]. Although a number of experimental and theoretical works have been done on different nanocrystalline materials, no work on compacted Fe-Ni invar nanocrystalline alloys could be found [13]. In this letter, the Fe-Ni nanocrystalline invar alloys were prepared by compaction and sintering of Fe-Ni nanoparticles. The effect of sintering temperature and compacting pressure on the microstructure and hardness of the nanocrystalline metals were studied.

The traditional arc discharge process has been used for synthesis of a number of metallic or oxide nanoparticles with different compositions [14,15]. In this work, we prepared Fe-Ni nanoparticles with arc discharge method and the effect of hydrogen concentration on the hydrogen plasma reaction products was investigated.

2. Materials and Methods

The Fe-Ni nanoparticles were prepared by using traditional arc discharge process analogous to our previous work [14,15]. The master invar alloy made by arc-melting of Fe and Ni powders (atomic ratio Fe:Ni = 61:39) served as anode while a tungsten needle served as a cathode. Several different samples were prepared by changing the electric current as well as the ratio between Ar and H₂ in the chamber. The as-prepared nanoparticles were characterized systematically by means of X-ray diffraction (XRD, D/max-γA; Rigaku, Tokyo, Japan) for structural analysis, transmission electron microscopy (TEM; JOEL, Tokyo, Japan) and scanning electron microscopy (SEM; JOEL, Tokyo, Japan) for morphology and microstructure analysis, X-ray photoelectron spectroscopy (XPS; Thermal Scientific ESCALAB 250, Waltham, MA, USA) for surface analysis, thermal gravity analysis and differential thermal analysis (Q600 SDT; TA Instruments, New Castle, DE, USA), respectively. The XRD and XPS measurements were carried out with CuK_α and AlK_α radiations, respectively.

In order to synthesize bulk Fe-Ni nanocrystalline invar alloys, we compacted the as-prepared Fe-Ni nanoparticles into 3 mm disks under 172, 682, and 1194 MPa, respectively. The compacted disks were then sintered in a tube furnace (Dongwon S.M., Dongwon, Korea) with flowing hydrogen as protection gas for 2 h at 600, 700, 800, and 900 °C, respectively. The microstructure of the sintered disks originally compacted under 172 MPa was studied by using TEM/SEM. The samples for microscopy observations were etched by swabbing the sample surface with Nital etchant (2% HNO₃ in ethanol). A microhardness tester (Jvjing, Shanghai, China) based on Vicker's principle was employed for testing micro-hardness. Tests were carried out at a load of 500 g. Each value for hardness was averaged from data based on 10 measurements. The density of the nanocrystalline Fe-Ni invar alloys was measured by using a hydrostatic balance.

3. Results and Discussions

3.1. Characterization of the Precursor Fe-Ni Nanoparticles

A composition deviation of the as-prepared nanoparticles with respect to their master alloy was frequently observed when the nanoparticles were prepared by co-evaporation process because of different vapor pressures of the components in the alloys. Therefore, a precise control on the composition of the nanoparticles is difficult. The "invar effect" in Fe-Ni alloys occurs when the Fe content approaches 65 at % [1,3]. In order to obtain Fe-Ni nanoparticles with compositions close to Fe₆₅Ni₃₅, we used Fe₆₁Ni₃₉ as master alloy in this work. The selection of the composition of the master alloy was based on [16], in which the composition deviation in iron-nickel system was investigated. By extrapolating the iron content in nanoparticles vs. that in bulk alloys, we estimated a 61 at % iron content in the master alloys [16]. For convenience, we hereafter refer to the as-prepared nanoparticles and their sintered alloys as Fe-Ni.

Figure 1 shows the morphology of the Fe-Ni nanoparticles prepared under different electric current and hydrogen concentration. Microscopy observations reveal that most of the Fe-Ni nanoparticles are spherical in shape. Particle size was investigated by manual counting of the particles. For same preparation atmosphere 50 kPa Ar + 50 kPa H₂, the average diameter of the nanoparticles prepared in 200 A (or 300 A) is (64 ± 9) nm (or (39 ± 7) nm). For the same preparation electric current 300 A and same total pressure 100 kPa, the average diameter of the nanoparticles prepared in 50 vol % (or 70 vol %) H₂ is (39 ± 7) nm (or (47 ± 6) nm). The particle size increases with increasing hydrogen content. According to the phase diagrams, at higher hydrogen pressures, the H solubility in both melting Fe and Ni increases, and the melting point of the metal is reduced. A lowered melting point indicates enhanced vapor pressure of the metal and thus an increased particle size as well as enhanced productivity, i.e., the mass of the nanoparticles produced in certain time intervals. In fact, the productivity of the nanoparticles had been observed to increase significantly with increasing hydrogen pressure in our experiments. The hydrogen dissolved in the melt metal releases as temperature declined. The release of the hydrogen would agitate the boiling melt when flowing from a high temperature region to a low temperature region. Then the productivity of nanoparticles was enhanced. The Fe-Ni invar alloy nanoparticles obtained by electrical exploration of wire in flowing nitrogen showed a similar morphology with their diameters being within the 3–150 nm range [17].

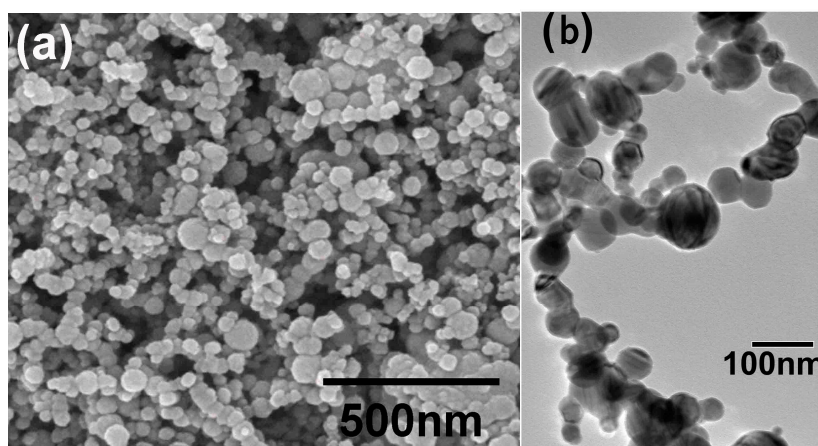


Figure 1. Morphology of the Fe-Ni nanoparticles prepared in 50 kPa Ar + 50 kPa H₂ with an electric current of (a) 200 A. Nanoparticles shown in (b) were prepared in 30 kPa Ar + 70 kPa H₂ with a current of 300 A. The particle size decreases with increasing current and decreasing hydrogen content.

The XRD patterns for the as-prepared Fe-Ni nanoparticles were shown in Figure 2a, revealing the formation of austenitic FCC (face centered cubic) structure in the Fe-Ni nanoparticles with lattice parameter of $(3.5998 \pm 0.0006) \text{ \AA}$, which is smaller than the $(3.6038 \pm 0.0007) \text{ \AA}$ in the Fe₆₁Ni₃₉ master alloy. The shift of the (200) diffraction peak indicates the composition deviation of the as-formed nanoparticles with respect to their master alloy, as shown in the inset of Figure 2a. No martensitic BCC (body centered cubic) structure and Fe₃Ni, which are expected at room temperature according to the equilibrium phase diagram of Fe-Ni alloys, were detected. The remarkable stabilization of austenitic phase at room temperature has also been observed in previous works while the origin remains unclear [16,18]. Li's work showed that BCC phase appeared at 60 at % Fe contents or higher [19]. However, no BCC phase was detected in our Fe-Ni nanoparticles, even though their Fe content is higher than 60 at %, indicating enhanced stability of the FCC phase in the nanoparticles. Similar enhanced stability has been studied in Fe-Ni alloys with higher Fe content [20]. Moreover, the absence of diffraction peaks for pure Fe and Ni indicates the formation of alloyed nanoparticles. It should be noted that we did not observe characteristic peaks for their oxides. However, detailed investigations by the following XPS measurements verified the presence of their oxides over the surface of these

nanoparticles. The absence of the X-ray diffraction peaks was attributed to a very small percentage or very small crystallite size of the oxides in the sample.

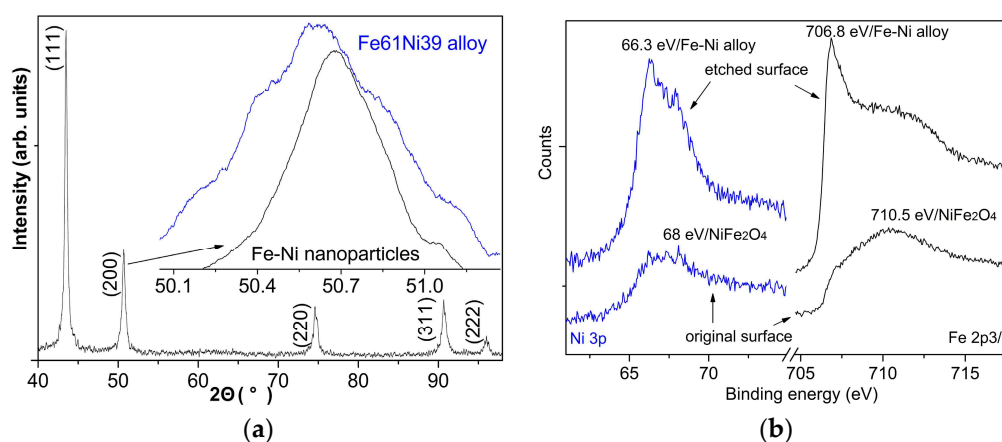


Figure 2. (a) The X-ray diffraction patterns of Fe-Ni nanoparticles prepared by arc evaporating $\text{Fe}_{61}\text{Ni}_{39}$ alloys. The inset shows reduced lattice parameters of Fe-Ni nanoparticles in comparison with that of the master $\text{Fe}_{61}\text{Ni}_{39}$ alloys. (b) the XPS (X-ray photoelectron spectra) of the Fe $2p^{3/2}$ and Ni 3p photoelectrons in the as-prepared Fe-Ni nanoparticles, the absence of the 66.3 and 706.8 eV peaks on the original surface indicates surface oxidation.

Figure 2b shows the XPS spectra of the Fe $2p^{3/2}$ and Ni 3p photoelectrons in the as-prepared Fe-Ni nanoparticles for the original surface and the surface after argon-ion etching for 600 s. The difference between the XPS spectra for the original surface and the etched surface is attributed to the oxidation of atoms on the surface of the particles when exposed to air. The sharp peak in Fe $2p^{3/2}$ spectra with binding energy of 706.8 eV (etched surface) should be the characteristic binding energy for Fe $2p^{3/2}$ photoelectrons in Fe-Ni invar alloys. Meanwhile, the broad peak in the vicinity of 710.5 eV is in good agreement with NiFe_2O_4 [21]. For Ni 3p spectra, the binding energy of 66.3 eV (etched surface) corresponds also to that in Fe-Ni invar alloys while a 68 eV peak arises from NiFe_2O_4 [22]. Therefore, we can conclude that the original surface of the as-prepared nanoparticles is mainly composed of NiFe_2O_4 while the core of the nanoparticles is Fe-Ni alloys.

3.2. Characterization of the Nanocrystalline Invar Alloys

The density of the nanocrystalline Fe-Ni invar alloys was shown in Table 1. For the sample annealed at 600 °C, the density increases with increasing compaction pressure. However, the density does not necessarily increase with increasing compaction pressure at sintering temperatures above 700 °C. Most samples sintered at temperatures above 700 °C show a high density near full density, containing less than 2% residual porosities.

The Vicker's hardness for the nanocrystalline alloys prepared at a variety of sintering temperatures and compaction pressures are shown also in Table 1. For the master alloy, a Vicker's hardness of 139.8 HV was measured for comparison. The invar alloys made by additive manufacturing process exhibited similar hardnesses of (141 ± 2.7) HV [4]. All the nanocrystalline alloys exhibited enhanced hardness. The most noticeable feature was that the hardness of the alloys prepared at 800 and 900 °C was lower than that of the alloy prepared at 700 °C. As mentioned above, the grain size increases with increasing temperature, and thus a smaller grain size indicates a higher fraction of grain boundaries. Normally, the boundaries are thought to play the role of barriers to dislocation motion, thus hindering deformation and increasing hardness. The relationship between the hardness and the preparation conditions seems to be complicated. A higher compaction pressure does not necessarily result in a higher hardness, even though very often it can increase the density. A lower sintering temperature might also decrease the hardness, even though usually it can decrease the grain size. We speculate that

the annealing time should be another important factor for the final grain size and density. The samples sintered at 600 °C and 1194 MPa exhibited the highest hardness of 242.2 HV. The effect of oxides on the hardness seems complicated. For high density samples (1194 MPa), the hardness of the samples decreases with increasing sintering temperature. However, for low density samples (172 and 682 MPa), the hardness of the samples increases first and then decreases with increasing sintering temperature.

Table 1. Density (%) and Vicker’s hardness (in parenthesis; unit: HV) of the nanocrystalline invar alloys prepared at varied temperatures and compaction pressures. Note that the Vicker’s hardness for the master alloy is 139.8 HV, which is much lower than that of most Fe-Ni nanocrystalline alloys shown here.

Pressure\Temperature	600 °C	700 °C	800 °C	900 °C
172 MPa	90.36%	98.11%	99.19%	97.71%
	(183 ± 3.1)	(222.8 ± 2.9)	(200 ± 3.5)	(180.5 ± 2.8)
682 MPa	97.74%	98.01%	99.32%	99.37%
	(214.9 ± 2.5)	(227.7 ± 3.0)	(214.7 ± 3.2)	(194.4 ± 2.7)
1194 MPa	98.78%	98.87%	98.88%	99.6%
	(242.2 ± 2.6)	(225.2 ± 2.8)	(207.7 ± 3.3)	(190.8 ± 2.9)

The microstructure of the nanocrystalline invar alloys prepared by sintering the Fe-Ni nanoparticles at different temperatures is shown in Figure 3. When annealed at 600 °C (Figure 3a), the nanoparticles became agglomerate but many are still remaining in different grains, i.e., the grains in the alloys are comparable in size to that of the precursor nanoparticles. Moreover, the combination of different nanoparticles seems to be weak and the alloys are porous. The low density (90.36%), as shown in Table 1, further proved the loose agglomeration when sintered at 600 °C. These pores are responsible for most of the lowered density. Figure 3b shows that after annealing the sample at 700 °C, the nanoparticles became rounded and larger. The growing of the nanoparticles reduced the porosity significantly. Most grains are smaller than 100 nm in their size while some others are larger than 100 nm. However, after annealing at 800 °C, the grain size shown in Figure 3c is much larger than that in Figure 3b (700 °C). The grain boundaries between different nanocrystalline grains are observed clearly in Figure 3b,c. Figure 3d shows the SEM micrograph of alloys obtained by sintering at 900 °C. The size of most grains ranges from several tens of nanometers to several hundreds of nanometers, which is apparently larger than that sintered at 800 °C. Bubble-like cavities (150–350 nm) were observed in the vicinity of the grain boundaries as shown in Figure 3d. We attribute the formation of these cavities to the concentration of the impurities (most probably surface oxides) in the nanoparticles during grain growth. Grain growth pushes impurities and residual gas to the boundaries. The residual gas being trapped in the boundaries induces the formation of these cavities when cooling down. The presence of these cavities might be one reason for the small density reduction of the samples (Table 1). Note that, apart from protecting the metal from oxidation, the hydrogen atmospheres have the further advantage of reducing the oxide on the surfaces of the nanoparticles. Since surface oxide usually increases with decreasing particle size, as here we use nanoparticles, the hydrogen is of great significance.

In order to know more about the sintering process of the samples, we performed thermal analysis on the compacted nanoparticles from room temperature to 1100 °C in air and Ar, respectively, as shown in Figure 4. When measured in air, the differential thermal analysis (DTA) spectra of the compacted Fe-Ni nanoparticles present a strong exothermic peak at 246 °C. Meanwhile, the exothermic peak corresponds to a rapid increase of the gravity, originating from air oxidation of the sample in this temperature range. The sample gravity stops increasing at 405 °C after a 5 wt % increase. Another rapid gravity increment occurs at temperatures above 750 °C. The gravity stabilization between 405 and 750 °C was ascribed to the protecting properties of the oxide layers originally formed on the surface of the samples.

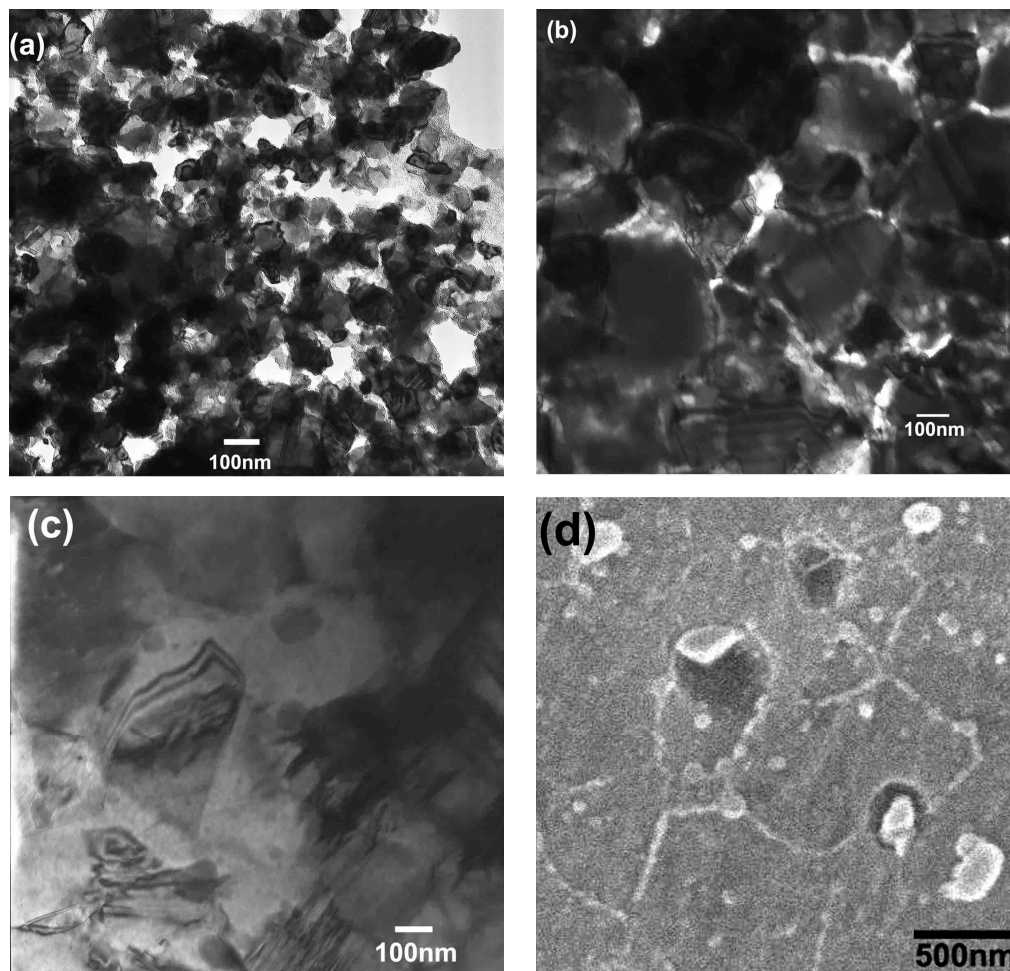


Figure 3. Micrographs of bulk nanocrystalline invar alloys prepared by sintering the 172 MPa-compacted Fe-Ni nanoparticles at (a) 600 °C, (b) 700 °C, (c) 800 °C, and (d) 900 °C for 2 h, respectively.

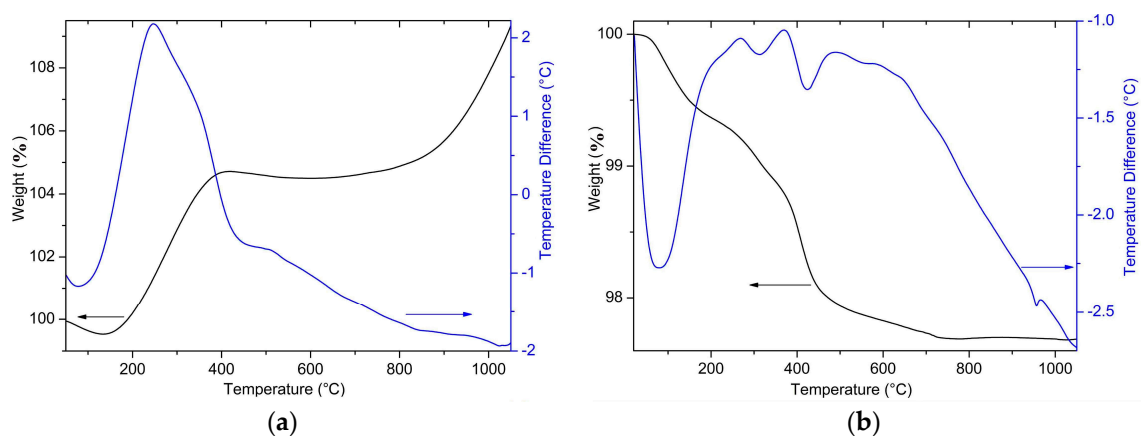


Figure 4. Differential thermal analysis (DTA—blue) and thermogravimetric analysis (TGA—black) for the Fe-Ni nanoparticles performed in (a) air and (b) argon, respectively. The heating rate is 20 K/min.

For the sample analyzed in argon, the gravity of the sample decreases monotonically with increasing temperature up to 735 °C. There are two possible reasons for the gravity reduction. One is physical process, including desorption of gases originally absorbed on the surface of the nanoparticles and evaporation of absorbed substances at elevated temperatures. The other reason may involve

chemical processes such as decomposition of impurities in the sample. Total gravity reduction of the sample is 2.3 wt %. Since both the physical and the chemical process might occur in the overall temperature range, it is difficult to distinguish the respective effect of these processes on the gravity quantitatively. However, in combination with the thermal analysis spectra, we can imagine the heating process qualitatively. The thermal curve reveals four endothermic peaks: one strong at about 77 °C and the others weak at about 313, 424, and 956 °C, respectively. A very broad exothermic peak could also be observed between 200 and 650 °C. We ascribe the 77 °C endothermic peak to the physical processes. Due to the large surface area, a large amount of gases and moisture were absorbed on the surfaces of the nanoparticles. At elevated temperatures, the desorption process and evaporation of the moisture might absorb energy. In fact, even for samples analyzed in air, a small reduction of the gravity and weak endothermic peak could also be observed at temperatures close to 77 °C. The peaks at 313 and 424 °C might associate with the chemical decomposition process of the oxide impurities because a rapid gravity reduction could also be seen at these temperatures. No gravity change was observed close to the 956 °C peak, and thus this peak indicates a phase transformation or a rapid merging of the nanoparticles. The broad exothermic peak between 200 and 650 °C was ascribed to the release of the energy stored in the defects or disordered region in the sample. As mentioned above, the rapid vapor deposition process makes the as-produced Fe-Ni nanoparticles a metastable phase, meanwhile defects and disordered regions are generated. When thermally activated, the defect relaxation would release the energy stored in the sample. The 735 °C gravity-stabilization temperature can, to some extent, explain why our sample sintered at 700 °C shows higher hardness. Below this temperature, the oxides, which are detrimental to the mechanical properties of alloys, over the surface of the nanoparticles could not be removed completely. Above this temperature, the grain size increases rapidly with increasing temperature. At temperatures close to the gravity-stabilization temperature, an oxide-free microstructure with small grain size is achieved. The fraction of oxide impurities in the precursor nanoparticles and the final products has substantial effects on the properties of the final products. It is difficult to control the impurities in the precursor nanoparticles which would be oxidized spontaneously on the surface when exposed to air. It is easier for us to control the oxide impurities by controlling the hydrogen reduction process, during which a complete removal of oxides without significant growth of grain size is crucial.

4. Conclusions

We have prepared nanocrystalline bulk metals and nanoparticles of Fe-Ni invar alloys. The particle size and the productivity of the Fe-Ni nanoparticles during arc discharge increased with increasing hydrogen pressure. No FCC to BCC structural transition was observed in the Fe-Ni nanoparticles due to the enhanced stability of the particles when in nanoscale. X-ray photoelectron spectra showed that the characteristic binding energy for Fe 2p^{3/2} and Ni 3p photoelectrons in Fe-Ni invar alloys is 706.8 and 66.3 eV, respectively. Moreover, the Fe-Ni nanoparticles were oxidized slightly on their surface when exposed to air. High-density nanocrystalline invar alloys with significantly enhanced hardness were prepared by sintering the compacted Fe-Ni nanoparticles in hydrogen.

Acknowledgments: We are grateful for support from the Future Materials Discovery Program through the National Research Foundation of Korea (NRF) funded by the Ministry of Science, ICT and Future Planning (No. 2016M3D1A1027835), and the National Natural Science Foundation of China (No. 11074227 and 51671177). Thanks are also given to Y.S.L., J.P., J.W.L., S.P.K., P.Y.P. and W.S.L. for their help in the experiments and manuscript editing.

Author Contributions: P.-Z.S. and C.-J.C. designed and conducted the experiments.

Conflicts of Interest: The authors declare no conflict of interest.

References

1. Guillaume, C.E. Recherches sur les aciers au nickel. Dilatations aux températures elevees; resistance electrique. *CR Acad. Sci.* **1897**, *125*, 235–238.

2. Qiu, C.; Nicholas, J.E.A.; Attallah, M.M. Selective laser melting of Invar 36: Microstructure and properties. *Acta Mater.* **2016**, *103*, 382–395. [[CrossRef](#)]
3. Schilfgaard, M.; Abrikosov, I.A.; Johansson, B. Origin of the Invar effect in iron-nickel alloys. *Nature* **1999**, *400*, 46–49. [[CrossRef](#)]
4. Bobbio, L.D.; Otis, R.A.; Borgogna, J.P.; Dillon, R.P.; Shapiro, A.A.; Liu, Z.K.; Beese, A.M. Additive manufacturing of a functionally graded material from Ti-6Al-4V to Invar: Experimental characterization and thermodynamic calculations. *Acta Mater.* **2017**, *127*, 133–142. [[CrossRef](#)]
5. Li, H.; Ebrahimi, F. Ductile-to-brittle transition in nanocrystalline metals. *Adv. Mater.* **2005**, *17*, 1969–1972. [[CrossRef](#)]
6. Nadutov, V.M.; Ustinov, A.I.; Demchenkov, S.A.; Svystunov, Y.O.; Skorodzievski, V.S. Structure and properties of nanostructured vacuum-deposited foils of Invar Fe-(35–38 wt %)Ni alloys. *J. Mater. Sci. Technol.* **2015**, *31*, 1079–1086. [[CrossRef](#)]
7. Park, H.K.; Hwang, N.M.; Park, Y.B. Abnormal grain growth in the nanostructured Invar alloy fabricated by electrodeposition. *Philos. Mag. Lett.* **2012**, *92*, 589–596. [[CrossRef](#)]
8. Liu, Y.; Liu, L.; Shen, B.; Hu, W. A study of thermal stability in electrodeposited nanocrystalline Fe-Ni Invar alloy. *Mater. Sci. Eng. A* **2011**, *18*, 5701–5705. [[CrossRef](#)]
9. Tjong, S.C.; Chen, H. Nanocrystalline materials and coatings. *Mater. Sci. Eng. R Rep.* **2004**, *45*, 1–88. [[CrossRef](#)]
10. Wu, X.J.; Du, L.G.; Zhang, H.F.; Liu, J.F.; Zhou, Y.S.; Li, Z.Q.; Xiong, L.Y.; Bai, Y.L. Synthesis and tensile property of nanocrystalline metal copper. *Nanostruct. Mater.* **1999**, *12*, 221–224. [[CrossRef](#)]
11. Haghighi, S.E.; Janghorban, K.; Izadi, S. Structural evolution of Fe-50 at. % Al powders during mechanical alloying and subsequent annealing processes. *J. Alloys Compd.* **2010**, *495*, 260–264. [[CrossRef](#)]
12. Haghighi, S.E.; Janghorban, K.; Izadi, S. Order-sintering of mechanically alloyed FeAl nanostructures. *J. Alloys Compd.* **2010**, *503*, 375–379. [[CrossRef](#)]
13. Peng, H.R.; Gong, M.M.; Chen, Y.Z.; Liu, F. Thermal stability of nanocrystalline materials: Thermal dynamics and kinetics. *Int. Mater. Rev.* **2017**, *62*, 303–333. [[CrossRef](#)]
14. Si, P.Z.; Jiang, W.; Wang, H.X.; Li, Z.F.; Liu, J.J.; Lee, J.G.; Choi, C.J. Large scale synthesis of nitrogen doped TiO₂ nanoparticles by reactive plasma. *Mater. Lett.* **2012**, *68*, 161–163. [[CrossRef](#)]
15. Si, P.Z.; Skorvanek, I.; Kovac, J.; Geng, D.Y.; Zhao, X.G.; Zhang, Z.D. Structural and magnetic properties of Gd nanoparticles and carbon coated Gd/GdC₂ nanocapsules. *J. Appl. Phys.* **2003**, *94*, 6779–6784. [[CrossRef](#)]
16. Duhamel, C.; Champion, Y.; Tence, M.; Walls, M. Synthesis of controlled-chemistry ultrafine Fe_xNi_{1-x} ferromagnetic powders. *J. Alloys Compd.* **2005**, *393*, 204–210. [[CrossRef](#)]
17. Kurlyandskaya, G.V.; Bhagat, S.M.; Bagazeev, A.V.; Medvedev, A.I.; Ballesteros, A.; Beketov, I.V.; Safronov, A.P. Structure, magnetic and microwave properties of FeNi Invar nanoparticles obtained by electrical explosion of wire in different preparation conditions. *J. Phys. Chem. Solids* **2016**, *98*, 255–262. [[CrossRef](#)]
18. Tadaki, T.; Murai, Y.; Koreeda, A.; Nakata, Y.; Hirotsu, Y. Structure and phase transformation of nano-scale particles of Fe-Ni alloys. *Mater. Sci. Eng. A* **1996**, *217–218*, 235–238. [[CrossRef](#)]
19. Li, X.G.; Chiba, A.; Takahashi, S. Preparation and magnetic properties of ultrafine particles of Fe-Ni alloys. *J. Magn. Magn. Mater.* **2005**, *170*, 339–345. [[CrossRef](#)]
20. Asaka, K.; Hirotsu, Y.; Tadaki, T. Martensitic transformation in nanometer-sized particles of Fe-Ni alloys. *Mater. Sci. Eng. A* **1999**, *273–275*, 262–265. [[CrossRef](#)]
21. McIntyre, N.S.; Zetaruk, D.G. X-ray photoelectron spectroscopic studies of iron oxides. *Anal. Chem.* **1977**, *49*, 1521–1529. [[CrossRef](#)]
22. McIntyre, N.S.; Cook, M.G. X-ray photoelectron studies on some oxides and hydroxides of cobalt, nickel, and copper. *Anal. Chem.* **1975**, *47*, 2208–2213. [[CrossRef](#)]

